



HAL
open science

The Electrical Conductivity of Liebermannite: Implications for Water Transport Into the Earth's Lower Mantle

Geeth Manthilake, Federica Schiavi, Chengcheng Zhao, Mainak Mookherjee,
Mohamed Ali M.A. Bouhifd, Laurent Jouffret

► **To cite this version:**

Geeth Manthilake, Federica Schiavi, Chengcheng Zhao, Mainak Mookherjee, Mohamed Ali M.A. Bouhifd, et al.. The Electrical Conductivity of Liebermannite: Implications for Water Transport Into the Earth's Lower Mantle. *Journal of Geophysical Research: Solid Earth*, 2020, 125 (8), 10.1029/2020JB020094 . hal-03008830

HAL Id: hal-03008830

<https://hal.science/hal-03008830>

Submitted on 17 Nov 2020

HAL is a multi-disciplinary open access archive for the deposit and dissemination of scientific research documents, whether they are published or not. The documents may come from teaching and research institutions in France or abroad, or from public or private research centers.

L'archive ouverte pluridisciplinaire **HAL**, est destinée au dépôt et à la diffusion de documents scientifiques de niveau recherche, publiés ou non, émanant des établissements d'enseignement et de recherche français ou étrangers, des laboratoires publics ou privés.

1 **The electrical conductivity of liebermannite: Implications for water transport into the**
2 **Earth's lower mantle**

3
4
5 Geeth Manthilake^{1*}, Federica Schiavi¹, Chengcheng Zhao¹, Mainak Mookherjee², Mohamed Ali
6 Bouhifd¹, Laurent Jouffret³

7
8 ¹ Laboratoire Magmas et Volcans, CNRS, IRD, OPGC, Université Clermont Auvergne,
9 63000 Clermont-Ferrand, France

10 ² Earth Materials Laboratory, Department of Earth, Ocean and Atmospheric Sciences, Florida State
11 University, Tallahassee, FL, 32306, USA

12 ³ Laboratoire des Matériaux et du Génie Physique, UMR 5628, 3 parvis Louis Néel - CS50257 -
13 38016 Grenoble, France

14
15 ***Corresponding author:** Geeth Manthilake (geeth.manthilake@uca.fr)

16
17
18 **Key Points:**

- 19 • The hopping of K⁺ ions in liebermannite results in high electrical conductivity of more
20 than 1 S/m.
- 21 • Water can be present as both molecular H₂O and hydroxyl (OH⁻) groups in liebermannite
- 22 • High H₂O contents of ocean island basalts can be related to deeply subducted hydrous
23 liebermannite

25 **Abstract**

26 Liebermannite (KAlSi_3O_8) is a principal mineral phase expected to be thermodynamically
27 stable in deeply subducted continental and oceanic crusts. The crystal structure of liebermannite
28 exhibits tunnels that are formed between the assemblies of double chains of edge-sharing (Si, Al)
29 O_6 octahedral units, which act as a repository for large incompatible alkali ions. In this study, we
30 investigate the electrical conductivity of liebermannite at 12, 15, and 24 GPa and temperature of
31 1500 K to track subduction pathways of continental sediments into the Earth's lower mantle.
32 Further, we looked at whether liebermannite could sequester incompatible H_2O at deep mantle
33 conditions. We observe that the superionic conductivity of liebermannite due to the thermally
34 activated hopping of K^+ ions results in high electrical conductivity of more than 1 S/m. Infrared
35 spectral features of hydrous liebermannite indicate the presence of both molecular H_2O and
36 hydroxyl (OH^-) groups in its crystal structure. The observed high electrical conductivity in the
37 mantle transition zone beneath Northeastern China and the lower mantle beneath the Philippine
38 Sea can be attributed to the subduction pathways of continental sediments deep into the Earth's
39 mantle. While major mineral phases in pyrolitic compositions are almost devoid of H_2O under
40 lower mantle conditions, our study demonstrates that liebermannite could be an important host of
41 H_2O in these conditions. We propose that the relatively high H_2O contents of ocean island basalts
42 derived from deep mantle plumes are primarily related to deeply subducted continental sediments,
43 in which liebermannite is the principal H_2O carrier.

44

45

46

47

48

49

50 **Plain Language Summary**
51

52 Liebermannite (KAlSi_3O_8 , formally K-hollandite) is an important mineral phase in deeply
53 subducted continental and oceanic crusts. Liebermannite exhibits high ionic conductivity and
54 could explain low resistivity in the Earth's mantle transition zone and the upper part of the lower
55 mantle, hinting towards the subduction of hydrated crusts into the lower mantle. The liebermannite
56 samples synthesized at these conditions indicate the presence of both molecular H_2O and hydroxyl
57 (OH^-) groups in its crystal structure, suggesting that liebermannite could be an important host of
58 H_2O in the Earth's deep mantle. Compared to the basalts from mid-ocean ridges that exhibit trace
59 quantities of water, ocean island basalts show higher water contents. It has been speculated that
60 ocean basalts are derived from crustal components that were deeply subducted. It is also known
61 that the lower mantle is relatively dry. Therefore, it is difficult to reconcile the higher water
62 contents in OIBs that are derived from the deep mantle. Here, we demonstrate that the source
63 crustal components for OIBs were likely to be hydrated. Liebermannite is a key mineral in deeply
64 subducted crusts and can efficiently host water.

65
66
67
68
69
70
71
72
73
74
75
76

77 1. Introduction

78 Trace quantities of H₂O stored in the Earth's mantle significantly influence the physical
79 properties of mantle rocks (Smyth & Jacobsen, 2006). Although H₂O plays an important role by
80 affecting both mineral properties and mantle dynamics of the upper mantle, it is well known that
81 the Earth's lower mantle is relatively dry, as indicated by the low (< 1000 ppm wt.) H₂O solubility
82 in major lower mantle mineral phases (Bolfan-Casanova et al., 2003; Fu et al., 2019; Hirschmann,
83 2006). Yet some oceanic island basalts (OIB), which are characterized by relatively high H₂O
84 contents up to ~ 2.0 wt. %, are fed by plumes rising from the lower mantle (Deschamps et al.,
85 2011). These plumes are thought to originate from enriched reservoirs composed of recycled
86 crustal materials that subducted into the deep mantle (Willbold & Stracke, 2006). Hydrous phases
87 associated with subducting slabs descending into the lower mantle (van der Hilst et al., 1997) may
88 provide a plausible mechanism for transporting H₂O into the deep mantle. Dense hydrous
89 magnesium silicates (DHMS), such as phase H and phase D, which are known to be stable in the
90 depleted portion of the subducting slab at lower mantle conditions, are likely to transport H₂O into
91 the lower mantle and subsequently hydrate the subducted crustal components (Nishi et al., 2014;
92 Pamato et al., 2014).

93 While the dominant component of all OIB is likely to be recycled basaltic oceanic crust,
94 both chemical and isotopic signatures of OIB indicate the mixing of different source materials
95 (Hart, 1988). Particularly the Enriched Mantle II (EMII)-type OIB, which have been found in the
96 Society Islands, the Marquesas and Samoa, suggest a 5-10 % of continental and sedimentary
97 components (Hart, 1988). Water contents up to 1.5 wt. % and low H₂O/Ce (<150) have been
98 reported in such EMI type OIB (Cabral et al., 2014). The estimates based on geochemical
99 analyses indicate that H₂O concentrations in EMII sources are about 400 ppm wt. (Dixon et al.,

100 2002). The low H₂O/Ce measured in EM-type magmas indicates up to 92 % H₂O loss from the
101 recycled continental components with progressive dehydration (Dixon et al., 2002). Despite
102 intense dehydration, the deeply subducted slab appears to retain or rehydrate by the dehydration
103 of dense hydrous phases such that a sufficient amount of H₂O is available in the deep OIB sources
104 (Dixon et al., 2002).

105 Liebermannite, formerly known as Liebermannite, is the high-pressure polymorph of
106 KAlSi₃O₈-feldspar and is likely to be stable in deeply subducted (> 300 km) continental crust and
107 mid-oceanic ridge basalt compositions enriched in potassium (Schmidt, 1996). The crystal
108 structure of liebermannite exhibits tunnels that are formed between the assemblies of double chains
109 of edge-sharing (Si, Al)O₆ octahedral units. At pressures ≤ 20-23 GPa, liebermannite (*lowP*)
110 crystallizes in a tetragonal (*I4/m*) space group symmetry, whereas above these pressures, the
111 tunnels are slightly squeezed, and the high-pressure polymorph of liebermannite (*hiP*) crystallizes
112 in a monoclinic (*I2/m*) space group symmetry (Ferroir et al., 2006; Nishiyama et al., 2005). These
113 tunnels accommodate incompatible cations such as Na, K, Sr, Ba, La, and Pb. A naturally
114 occurring liebermannite containing Ba²⁺ and K⁺ is reported to contain up to 5 wt. % H₂O in its
115 crystal structure (Miura, 1986), indicating that liebermannite could be an important host for H₂O.
116 The *hiP* polymorph is observed to be stable down to the Earth's lowermost mantle conditions
117 (Kawai & Tsuchiya, 2013; Sueda et al., 2004). At mantle transition zone conditions, phase
118 equilibria studies indicate that average continental crust is composed of a mixture of liebermannite
119 (~32 vol. %), stishovite (24 vol.%), majoritic garnet (30 vol. %) and minor amounts of calcium
120 aluminosilicate (CAS) phases (Irifune et al., 1994).

121 The presence of tunnels in the crystal structure of liebermannite facilitates the motion of
122 K⁺ ions along the channel, attaining superionic conduction at high temperatures (Furusawa et al.,

123 1988; Khanna et al., 1981; Yoshikado et al., 1982). More recently, the electrical conductivity of
124 liebermannite, relevant for the deeply subducted crust, has been examined using molecular
125 dynamics simulations. The predicted electrical conductivity for liebermannite with a 12.5 %
126 vacancy in the tunnel is ~20 S/m at 10 GPa and 1600 K (He et al., 2016). The magnitude of the
127 predicted electrical conductivity resulting from ionic conduction of K^+ ions in the tunnels is
128 significantly greater than that of the electrical conductivity due to extrinsic defects. Hence, owing
129 to its high electrical conductivity, liebermannite potentially represents an ideal tracer mineral for
130 tracking subducted pathways of continental crustal components into the Earth's lower mantle.

131 The unique crystal structure of liebermannite and the ability to accommodate large alkali
132 ions and possibly H_2O in its tunnels highlight its importance as a possible H_2O repository in the
133 subducted crustal components and a possible source for OIB. However, so far, studies on
134 liebermannite have been restricted to the equation of state, elasticity (Caracas & Boffa Ballaran,
135 2010; Kawai & Tsuchiya, 2013; Mookherjee & Steinle-Neumann, 2009), and electrical
136 conductivity (He et al., 2016) of the dry variety.

137 In this study, we first conducted high-pressure and temperature experiments to constrain
138 the electrical conductivity of hydrous liebermannite at the upper mantle, transition zone, and lower
139 mantle conditions, i.e., at pressures of 12, 15, and 24 GPa respectively. Then we examined the
140 water incorporation mechanisms in liebermannite. Finally, we explore whether the high H_2O
141 contents of OIB could have derived from hydrated crustal components of deeply subducted slabs
142 penetrated down to the lower mantle.

143

144

145

146 **2. Materials and Methods**

147 The starting powder was prepared using high purity oxide mixtures of K_2CO_3 , Al_2O_3 , and
148 SiO_2 . The mixture was slowly heated to 1000 °C overnight in a platinum crucible for decarbonate
149 K_2CO_3 . The decarbonated powdered mixture was then heated to 1500 °C and kept 10 minutes to
150 obtain homogeneous glass. The time was optimized to avoid possible K loss at high temperatures.

151 High pressure-high temperature experiments were conducted using a 1500-ton multi-anvil
152 apparatus. The pre-synthesis of K-feldspar for electrical conductivity measurements were
153 conducted at 2 GPa and 1200 K in a 14/8 assembly (Fig. 1a). To synthesize hydrous K-feldspar we
154 add $Al(OH)_3$ to the glass mixture to obtain ~ 100 wt. ppm H_2O . The powdered mixture was packed
155 into a capsule made of rhenium (Re), and kept at high-pressure and high-temperature for durations
156 of 4 hours to obtain the cylindrical samples for electrical conductivity measurements. The water
157 contents of K-feldspar is measured to be 257 ± 29 wt. ppm.

158 The pressure and temperature conditions for the electrical conductivity measurements were
159 carefully chosen based on the stability of liebermannite (Nishiyama et al., 2005) and represent the
160 upper mantle (12 GPa), mantle transition zone (15 GPa), and the upper part of the lower mantle
161 (24 GPa). Electrical conductivity measurements were performed using octahedral pressure
162 medium composed of MgO and Cr_2O_3 (5 wt. %) in a 14/8 assembly (octahedron edge length/anvil
163 truncation edge length) at 12 GPa, in a 14/6 assembly at 15 GPa, and a 10/4 assembly at 24 GPa
164 (Fig.1b). MgO ceramic sleeves insulated the electrode wires from the furnace. All ceramic
165 assembly parts, including the pressure media, were baked at 1000 °C for more than 12 hours and
166 then stored at 125 °C in high-vacuum furnaces (< 100 mTorr) before assembling. This step
167 reduces the exposure of assembly components to atmospheric moisture and other impurities. The
168 sample temperature was measured using a type-C tungsten-rhenium (W95Re5-W74Re26)

169 thermocouple junction, placed at one end of the sample. One cable formed the thermocouple and
170 a separate W₉₅Re₅ cable placed at the opposite side of the sample connected to the impedance
171 spectroscopy for the electrical conductivity measurements.

172 The electrical conductivity of liebermannite samples was determined using the impedance
173 spectroscopy method using the Modulab MTS Impedance gain-phase analyzer. The frequency
174 range for the analyses was 10⁶-10¹ Hz. After compressing the assembly to the desired pressure,
175 samples were heated to 500 K and while maintaining a temperature of 500 K, the electrical
176 resistance of the sample was measured regularly until the sample resistance reached a stable value.
177 The decrease of electrical resistance observed at this step corresponds to the removal of the
178 absorbed moisture in the sample capsule and the surrounding area, which could be incorporated
179 into the sample at higher temperatures (Manthilake et al., 2015). During the measurements, sample
180 resistance was determined in several heating and cooling cycles until the electrical resistance of
181 heating and cooling paths become reproducible. For the discussion, we have used the data from
182 the last cooling cycle, which minimizes the uncertainty in electrical conductivity. The sample
183 resistance can be obtained by fitting the impedance spectra with an appropriate equivalent circuit.
184 For polycrystalline samples, as we use in this study, the equivalent circuit can be illustrated by a
185 combination of resistor-capacitor/constant phase element (R-C/CPE) components, connected in
186 parallel, series, or a series-parallel combination. Once the electrical resistivity of the samples was
187 determined from the fit of the impedance spectra, the electrical conductivity was determined using
188 the radius and the axial length of the cylindrical sample measured after each experiment. The
189 inherent assumption is that the sample geometry remained constant during the experiment.

190 The chemical compositions the experimental run products were investigated using a
191 Cameca SxFiveTactis electron probe microanalyzer (EPMA) in wavelength dispersive (WDS)

192 mode operating at an accelerating voltage of 15 kV and 4 nA beam current. The low accelerating
193 voltage was used to avoid the K loss in liebermannite.

194 Powder X-ray diffraction (PXRD) analyses of experimental run products were carried out
195 to identify the crystal structures of liebermannite and the phases present in quenched samples at
196 15 and 24 GPa. The PXRD was obtained for $\sim 1 \text{ mm}^3$ of crushed samples that were placed on zero-
197 background Si sample holders. The PXRD was recorded using a Philipps X-Pert Pro diffractometer
198 with $\text{CuK}\alpha$ radiation source ($\lambda = 0.15405 \text{ nm}$). The PXRD patterns were recorded over the $10\text{--}90^\circ$
199 (2θ) range in steps of 0.0167° with a counting time of 700 s per step. Lattice parameters were
200 obtained from LeBail fits using the FULLPROF program (Rodriguez-Carvajal, 1993). The
201 background can be obtained by linear interpolation between twenty-six points, and the peak
202 profiles were modeled using a pseudo-Voigt function.

203 Raman spectroscopy was used to identify liebermannite and the minor mineral phases
204 present in the experimental run products. Raman spectra were collected in a back-scattered
205 geometry using an InVia confocal Raman micro-spectrometer, equipped with a 532 nm diode laser,
206 a Peltier-cooled CCD detector, a Rayleigh rejection edge filter (Schiavi et al., 2018). The laser
207 power of 1-8 mW; the slit aperture of $65 \mu\text{m}$, and a grating of 2400 l/mm were used for the present
208 analyses. These conditions result in lateral and axial spatial resolutions of ~ 1 and $3 \mu\text{m}$ and a
209 spectral resolution of 1 cm^{-1} . Acquisition times were 30-60 s and 60-240 s for the low-wavenumber
210 and high-wavenumber region, respectively.

211 The quantification of H_2O in liebermannite was performed using the Fourier Transform
212 Infrared (FTIR) spectroscopy. Unpolarized FTIR spectra of liebermannite were acquired using a
213 Vertex70 Bruker spectrometer equipped with a Globar light source, a KBr beamsplitter, and an
214 MCT (Mercury-Cadmium-Tellurium alloy) detector. The beam size for the analyses was $\sim 30 \mu\text{m}$.

215 The spectra were obtained through a CaF₂ window with a resolution of 4 cm⁻¹. About 2000 scans
 216 were accumulated for a single spectrum. Thin slabs were cut perpendicular to the compression axis
 217 of the experimental run products using a high-precision diamond wire saw and polished using
 218 diamond mats without acetone or bond materials, such as crystal-bond or orthodontic adhesive
 219 paste to avoid IR signal contaminations. Being the samples polycrystalline, it was not possible to
 220 perform polarized measurements on single crystals; therefore, we estimated the H₂O content of
 221 each sample based on several spectra that were taken over many randomly oriented crystals. The
 222 spectra were integrated between 2600 and 3800 cm⁻¹, an average of several spectra was calculated
 223 for each sample and multiplied by a factor 3. The OH content was quantified using the Beer-
 224 Lambert law:

$$225 \quad C_{\text{H}_2\text{O}} = 18.02 \times A \times 10^6 / \varepsilon \times t \times \rho$$

226 where C_{H₂O} is the concentration of hydrous species expressed in ppm H₂O by weight, 18.02 is the
 227 molecular weight of H₂O; A is the total integrated area of bands in the region of interest, *t* is the
 228 thickness of the sample in cm, ε is the molar absorption coefficient, and ρ is the density of the
 229 sample in g/L. For the estimation of H₂O content in liebermannite, we used the theoretically
 230 predicted integral molar absorption coefficient of 250000 L/(mol.cm²) (Koch-Müller & Rhede,
 231 2010).

232

233 **3. Results**

234 The electrical conductivity of liebermannite samples at 12, 15, and 24 GPa are summarized
 235 in **Fig. 2**. The discontinuous increase in electrical conductivity at a temperature above 660 K during
 236 the first heating cycle of the 12 GPa experiment coincides with the transformation of K-Feldspar
 237 to liebermannite with increasing temperature (**Fig. 2a**). This transformation accounts for more than

238 one order of magnitude increase of conductivity for liebermannite. After the complete
239 transformation, the electrical conductivity of liebermannite increases with increasing temperature
240 from 700 K to 1500 K and reached to about 1 S/m at 12 GPa and 1500 K. The increase of pressure
241 appears to have an inverse effect on the electrical conduction in liebermannite (**Fig. 2b**). The
242 impedance spectra of the sample undergoing K-feldspar to liebermannite transition with increasing
243 temperature are shown (**Fig. 3**).

244 The activation enthalpy (ΔH) of each conduction mechanism can be calculated by fitting
245 the data to equation, $\sigma = \sigma_0 \exp(-\Delta H/RT)$, where σ is the electrical conductivity (S/m), T is the
246 absolute temperature (K), σ_0 is the pre-exponential factor (S/m), and R is the gas constant (J/K
247 mol). Here, we analyzed the activation enthalpy, first by manually fitting different temperature
248 segments to the fitting equation and, second, by fitting the equation to the entire temperature range
249 (Fei et al., 2020). The estimated activation enthalpies for different conduction mechanisms obtained
250 using two fitting methods are listed in **Table 1**.

251 The EPMA, SEM, and Raman grid-analyses indicate that liebermannite is the principal
252 phase present in samples synthesized at 12, 15, and 24 GPa (**Fig. 4**). However, minor amounts of
253 wadeite, kyanite, and stishovite presence in our samples, an observation consistent with a previous
254 study (Urakawa et al., 1994) (**Table. 2**) (**Fig.5**). The grid analyses with a step size of 5 μm also
255 confirmed the absence of melt in our samples. The minor phases mostly occur as isolated grains
256 within the liebermannite matrix (**Fig 5a**) and the volume fraction of minor phases appeared to
257 decrease with increasing pressure. Chemical analyses of minor phases at the 24 GPa sample were
258 hampered by either absence of minor phases (e.g kyanite) at high-pressure samples or if present,
259 their extremely small grain sizes ($< 5\mu\text{m}$).

260 The FTIR analyses of liebermannite samples after the electrical conductivity measurements
261 indicate water contents of 1044 ± 87 wt. ppm at 12 GPa, 885 ± 78 wt. ppm at 15 GPa and 1104 ± 18
262 wt. ppm at 24 GPa (**Fig 6**). The high water contents compared to the K-feldspar starting material
263 suggest that the absorbed moisture in the assembly parts may have been incorporated into the
264 sample during the K-feldspar-liebermannite transformation at high-temperature, yielding high
265 water contents in the liebermannite samples (i.e. higher than the amount of water produced by the
266 decomposition of $\text{Al}(\text{OH})_3$). We were not able to produce water-free liebermannite samples even
267 with dry pressure materials.

268 The infrared spectra provide information on water incorporation in liebermannite (**Fig. 6**).
269 Several O-H vibrational modes are observed: (1) the stretching vibrations of weakly hydrogen
270 bound hydroxyl units produce intense bands between 3700 and 3500 cm^{-1} ; these modes are more
271 pronounced in the 12 GPa sample. (2) The stretching vibrations of both H_2O molecules and more
272 strongly hydrogen bound hydroxyl units occur in the 3425 - 3100 cm^{-1} wavenumber range; they
273 become dominant in the 15 and 24 GPa samples (**Fig. 6a**). (3) The O-H stretching and bending
274 vibrations of the hydronium (H_3O^+) ion are observed near 2900 cm^{-1} and 1665 cm^{-1} ; these modes
275 disappear at the highest pressure. In the absence of organic contaminants, such as acetone or bond
276 materials, the coexistence of these two modes confirms the presence of H_3O^+ in *lowP*
277 liebermannite. (4) The H-O-H bending vibration of the water molecule slightly shifts from 1610
278 to 1630 cm^{-1} with increasing pressure (**Fig. 6b**). (5) The combination (stretching/bending) modes
279 of both H_2O molecules (near 5200 cm^{-1}) and hydroxyl units (near 4500 cm^{-1}) display continuous
280 shift to lower frequencies with increasing pressure (**Fig. 6c**). This shift is compatible with the
281 increase of the strength of hydrogen bonds with pressure, as usually observed in minerals (Cynn
282 & Hofmeister, 1994). The observed spectral features suggest the presence of H_2O and H_3O^+

283 substituting for K^+ in the tunnel (Bethell & Sheppard, 1953) and the substitution of hydrogen (H^+)
284 in octahedral sites where it forms O-H bonds with one of the six possible oxygen ions in the vacant
285 octahedral site.

286 The powder X-ray diffraction analyses were conducted on the samples synthesized at 15
287 GPa and 24 GPa. Both patterns can be refined with parameters consistent with the $I4/m$ phase:
288 $a = 9.3304(4)\text{\AA}$, $c = 2.7223(2)\text{\AA}$. Obtaining the same lattice parameters for the samples out of the
289 different pressures of annealing experiments implies that the liebermannite phase is elastic enough
290 to regain its low-pressure parameters consistent with previous studies (Nishiyama et al., 2005;
291 Sueda et al., 2004).

292

293 **4. Discussion and conclusions**

294 **4.1 Electrical conduction in liebermannite**

295 The electrical conductivity of K-feldspar before transforming into liebermannite exhibit
296 higher electrical conductivity compared to the previous electrical conductivity measurements of
297 F-feldspar reported at 1 GPa (Hu et al., 2013). The high electrical conductivity of K-feldspar
298 observed in our study can be explained by the 0.02 wt. % H_2O contents in our samples, compared
299 to the dry verity reported by Hu et al. 2013 study. Similar electrical behavior has been observed in
300 dry albite and water-bearing albite (Hu et al., 2013; Ni et al., 2011).

301 The electrical conductivity of hydrous liebermannite increases discontinuously upon
302 increasing temperature (**Fig. 2b**). At temperatures below 700 K, conductivity is likely to be
303 dominated by molecular water that is loosely bound in the tunnel sites and the associated activation
304 energy is less than 0.40 eV. In the temperature range between 700 K and 1100 K, the conductivity
305 is likely largely due to extrinsic proton defects that are formed due to coupled substitutions of the

306 octahedral sites. The associated activation energy varies between 0.64 eV and 0.78 eV. At
307 temperatures above 1200 K, the conductivity is likely to be dominated by fast motions of K^+ or H^+
308 ions (from H_3O^+) ions in the channel. The associated activation energy is greater than 0.82 eV.
309 Higher conductivity has also been observed in alkali bearing materials with the hollandite crystal
310 structure (Khanna et al., 1981). Such higher conductivity is often referred to as super-ionic
311 conductivity (He et al., 2016; Khanna et al., 1981). In our study, we are documenting such effects
312 at extreme pressures of 12 to 24 GPa in liebermannite.

313 The electrical conductivity of minor phases, wadeite, stishovite, and kyanite should not
314 interfere with the measured conductivity of liebermannite due to their low volume fractions (occur
315 as isolated grains). Based on chemical analyses of individual liebermannite grains in our samples,
316 we observe a maximum of 7 % K^+ site vacancy in our liebermannite after electrical conductivity
317 measurements at 12, 15, and 24 GPa. The intrinsic defects seem to dominate the conduction
318 mechanism at high temperatures, whereas extrinsic defects may be responsible for the observed
319 conductivity at lower temperatures.

320

321 **4.2 Water incorporation in liebermannite**

322 The occurrence of several OH stretching bands (Fig. 4a) suggests that different substitution
323 mechanisms take place, including H^+ substitution in octahedral sites and H_2O/H_3O^+ in tunnels,
324 resulting in distinct hydrogen bonding strengths. Protons attachment to both bridging and non-
325 bridging oxygen can also help to explain such a wide range of OH stretching vibrations. Strong
326 pleochroism in the $3500\text{-}3600\text{ cm}^{-1}$ range of the polycrystalline sample at 12 GPa indicates the
327 random orientation of the crystals, in contrast to higher pressure samples. Water/hydrogen could
328 be incorporated in liebermannite structure in a variety of sites including the substitution of H^+ in

329 the silicon octahedral sites, i.e., $\text{Si}_{\text{Si}}^{4+} = \text{Al}_{\text{Si}}^{3+} + \text{H}_{\text{Si}}^{1+}$ or $\text{Si}_{\text{Si}}^{4+} = 4\text{H}_{\text{Si}}^{1+}$, the substitution of H^+ in the
 330 aluminum octahedral site $\text{Al}_{\text{Al}}^{3+} = 3\text{H}_{\text{Al}}^{1+}$, the substitution of H^+ and H_3O^+ in the potassium site
 331 ($\text{K}_{\text{K}}^{1+} = \text{H}_{\text{K}}^{1+}$, or $\text{K}_{\text{K}}^{1+} = (\text{H}_3\text{O})_{\text{K}}^{1+}$) and accommodation of molecular H_2O in the tunnel as in
 332 $\text{KAlSi}_3\text{O}_8 + \text{H}_2\text{O} = \text{KAlSi}_3\text{O}_8 \cdot \text{H}_2\text{O}$. The chemical analyses provide crucial information on possible
 333 coupled substitution mechanisms for hydrogen incorporation in liebermannite. The slight
 334 deficiency in silicon and increase in aluminum observed in some liebermannite grains
 335 ($\text{K}_{0.957 \pm 0.044} \text{Al}_{1.090 \pm 0.057} \text{Si}_{2.931 \pm 0.032} \text{O}_8$) is consistent with a reaction involving a substitution in the
 336 distorted octahedral with the direct replacement of Si^{4+} by Al^{3+} and H^+ or by 4H^+ . The chemical
 337 analyses also indicate a slight aluminum deficiency in some crystals ($\text{K}_{1.00} \text{Al}_{0.983} \text{Si}_{3.01} \text{O}_8$). This
 338 may suggest possible proton substitution in the octahedral site, replacing Al^{3+} with 3H^+ .

339 As the *hiP* liebermannite is considered the dominant polymorph throughout the Earth's
 340 lower mantle, knowledge on water solubility in the *hiP* structure becomes crucial to assess the
 341 transport of H_2O to the deepest lower mantle regions through deep extending slabs. Given the
 342 positive clapeyron slope of P (GPa) = $16.6 + 0.007 K$ (T) between the *lowP* and *hiP* liebermannite
 343 and assuming that trace quantity of water is unlikely to affect the slope, the hydrous liebermannite
 344 sample synthesized at 24 GPa and 1500 K is expected to be the *lowP* polymorph with tetragonal
 345 symmetry (Nishiyama et al., 2005). However, upon a decrease of temperature to 1000 K, at
 346 constant pressure, the sample is likely to transform to *hiP* liebermannite with monoclinic symmetry
 347 (Nishiyama et al., 2005). Upon structural transformation from *lowP* to *hiP* liebermannite, the
 348 electrical resistivity measurements of the sample do not indicate a discontinuous decrease of the
 349 electrical resistance, which indicates the release of free fluid phase or hydrous melting in the
 350 sample (Freitas & Manthilake, 2019). Assuming that the water incorporation into the liebermannite
 351 structure occurs at the highest temperature, this crucial observation suggests that the *hiP*

352 liebermannite structure is capable of sequestering H^+ into octahedral sites as molecular H_2O or
353 ionic H_3O^+ in its structure similar to the *lowP* liebermannite. The incorporation of H_2O has been
354 observed in both naturally occurring tetragonal and monoclinic hollandite crystal structures with
355 different stoichiometry (Miura, 1986), thus confirming our observations on liebermannite. The
356 micro Raman grid-analyses of our samples after electrical conductivity measurements indicate the
357 absence of melt phases, confirming that the water expulsion may not occur in our samples at high
358 temperatures.

359 Due to the small grain sizes ($< 5 \mu m$), infrared analyses in these minor phases were not
360 possible; nevertheless, absence of peaks in the high-wavenumber region of the Raman spectra of
361 wadeite and Al-free stishovite indicates that water is not present within their crystal structure (**Fig.**
362 **7**). However, H_2O contents up to 3 wt. % have been observed in stishovite containing aluminum
363 (Litasov et al., 2007; Yoshino et al., 2014). IR spectral features of Al-free stishovite exhibit some
364 similarities with those of liebermannite in the spectral range from 3111 to 3261 (Litasov et al.,
365 2007). Particularly peak position of 3117 cm^{-1} in the sample synthesized at 15 GPa (**Fig. 7a**)
366 overlaps the main peak position of stishovite at 3117 cm^{-1} observed for Al- free and Al-bearing
367 stishovite (Yoshino et al., 2014). In order to confirm that the spectral feature at 3117 cm^{-1} in
368 liebermannite, we have analyzed the O-H region of the Raman spectra of stishovite in the 15 GPa
369 sample. The observed water-free conditions (**Fig 7a**) strongly suggests the spectral feature at 3117
370 cm^{-1} observed in liebermannite could be unrelated to stishovite, rather a spectral feature
371 characteristic of liebermannite. We conclude that the similarities between liebermannite and stishovite
372 may be related to similar substitution mechanisms of hydrogen in octahedral sites SiO_6 or AlO_6 .
373 The preferential partitioning of water into the liebermannite phase over stishovite observed in our
374 samples may be partly due to the low Al content in stishovite that is in equilibrium with

375 liebermannite (**Table 2**). Therefore, the presence of Al-free stishovite in the studied samples
376 should not influence the IR spectra of liebermannite. Even in the case of very low water contents
377 of about 16-30 wt. ppm observed in Al-free stishovite (Litasov et al., 2007), these should not affect
378 water quantification of liebermannite in this study.

379

380 **4.3 Geophysical implications**

381 The upper mantle underneath the Philippine Sea (Tarits & Mandéa, 2010) and Northeastern
382 China (Kelbert et al., 2009) is characterized by unusual electrical and seismic wave velocity
383 structures, in particular, electrical conductivities as high as 1 S/m and high-velocity anomalies of
384 up to $+\delta V_P$ 1.5 % and δV_S 2.0 % have been observed in these regions. The observed anomalies
385 cannot be readily explained by normal mantle consisting of major mantle phases such as olivine
386 and wadsleyite (Manthilake et al., 2009). If the observed positive velocity anomalies were assumed
387 to be caused by temperature variations alone, the temperature in the uppermost region of the mantle
388 transition zone estimated to be about 800 K below the normal mantle geotherm (Manthilake et al.,
389 2009). The corresponding electrical conductivity of hydrous olivine and wadsleyite for such low
390 temperatures would be significantly lower; as a consequence, the proton conduction in olivine and
391 wadsleyite cannot be responsible for the electrical conductivity observed at the upper mantle and
392 in the mantle transition zone (Manthilake et al., 2009). Similarly, the presence of melt cannot
393 explain the observed anomalies, because even a minor fraction of melt would significantly
394 decrease both the primary (V_P) and secondary (V_S) wave velocities (Chantel et al., 2016; Freitas
395 et al., 2017; Weidner et al., 2018).

396 Due to superionic conduction properties and high modal abundance (> 30 vol. %) of
397 liebermannite in deeply subducted crustal components, the electrical conduction in slabs is likely

398 to dominate by the liebermannite. This would make such slab components highly conductive
399 compared to slabs consisting of mafic and ultramafic lithologies (Huang et al., 2005; Yoshino et
400 al., 2008, 2008, 2014). However, the presence of liebermannite alone cannot account for the
401 positive velocity anomaly observed in the upper mantle beneath the Philippine Sea (Tarits &
402 Mandéa, 2010) and northeastern China (Kelbert et al., 2009) because the elastic wave velocities
403 measured in liebermannite are comparable with those of common mantle mineral phases (Caracas
404 & Boffa Ballaran, 2010; Mookherjee & Steinle-Neumann, 2009). Instead, the seismic wave
405 velocities of Al-poor stishovite, another principal mineral phase stable in subducting continental
406 sediments, are notably faster than those of mantle mineral phases (Gréaux et al., 2016). The
407 stishovite co-existing with liebermannite in our samples is noticeably devoid of aluminum (**Table**
408 **2**). Here we propose that Al-poor stishovite coexisting with liebermannite in the subducted
409 continental sediments may be responsible for the positive velocity anomaly observed at the mantle
410 transition zone beneath the Philippine Sea (Tarits & Mandéa, 2010) and northeastern China
411 (Kelbert et al., 2009).

412 Continental crustal portion of the subducted slab, consisting of liebermannite, majoritic
413 garnet, and stishovite, are expected to have a higher 0.2 g cm^{-3} density than the ambient mantle,
414 but this density relation is overturned at the 660 km discontinuity (Irifune et al., 1994; Nishiyama
415 et al., 2005). This implies that subducting crustal components of the slabs may penetrate into the
416 mantle transition zone, but are prevented from entering the lower mantle (Nishiyama et al., 2005),
417 such as those observed in the Northeastern China subduction system (Ichiki et al., 2006). However,
418 the lower mantle origin of some of the plumes (French & Romanowicz, 2015; Hart et al., 1992)
419 carrying the EM-type components in OIB magmas (Hart et al., 1992) provides strong evidence
420 supporting the presence of recycled continental materials in the lower mantle. We propose that

421 mixing of continental with oceanic sediments may increase the density of sedimentary components
422 facilitating the sinking of slabs towards the core-mantle boundary. The high electrical conductivity
423 observed at a 1200 km depths in the Earth's lower mantle beneath the Philippine sea subduction
424 system (Kelbert et al., 2009; Tarits & Mandéa, 2010) may be linked to such continuous subduction
425 of continental sediments across the mantle transition zone into the Earth's lower mantle (**Fig. 7**).

426 Owing to hotter temperatures relative to the ambient mantle, the rising plume is unlikely
427 to exchange incompatible elements, including water, with the surrounding mantle, including the
428 hydrated MTZ and the upper mantle (Bercovici & Karato, 2003). Thus, it is likely that the H₂O
429 present in plume-derived rocks is primarily linked to the deep lower mantle source. The relatively
430 high H₂O contents of OIB derived from deep mantle plumes hint towards the presence of hydrated
431 crustal components present in the deeper part of the lower mantle (**Fig. 8**). While major mineral
432 phases in pyrolitic compositions are almost devoid of H₂O under lower mantle conditions, our
433 study demonstrates that liebermannite could be an important host of H₂O in the Earth's lower
434 mantle. In this scenario, H₂O in the EMII-source OIB is primarily related to deeply subducted
435 continental materials, in which liebermannite is the principal H₂O carrier. On the other hand, the
436 subducted continental materials that may reach the core-mantle boundary would hydrate the HIMU
437 type plume sources together with a possible contribution from *dense hydrous magnesium silicates*
438 (DHMS) (Nishi et al., 2014; Pamato et al., 2014) and primordial H₂O (Dixon et al., 2002).

439

440

441

442

443

444 **Acknowledgments**

445 We thank Nathalie Bolfan-Casanova and Maud Boyet for constructive discussion, J-L. Devidal for
446 his assistance with electron microprobe analyses and Emmy Voyer for her assistance with SEM
447 analyses. The constructive and in-depth reviews by the associate Editor, and two reviewers: Lidong
448 Dai and Hongzhan Fei substantially improved the quality of the manuscript. G.M. acknowledges
449 funding from the(INSU-CNRS. M.M. is supported by the US National Science Foundation grants,
450 EAR 1753125, 1763215. This research was financed by the French Government Laboratory of
451 Excellence initiative n°ANR-10-LABX-0006, the Région Auvergne, and the European Regional
452 Development Fund (ClerVolc contribution number xx). The authors comply with AGU's data
453 policy, and the data of this study are available in Figshare.

454 (https://figshare.com/articles/Water_content_calculations/12179067)

455 and (https://figshare.com/articles/Experimental_data_xlsx/12179046).

456 The authors declare no competing financial interests.

457

458 **References**

459 Bercovici, D., & Karato, S.-I. (2003). Whole-mantle convection and the transition-zone water
460 filter. *Nature*, *425*(6953), 39–44. <https://doi.org/10.1038/nature01918>

461 Bethell, D. E., & Sheppard, N. (1953). The Infrared Spectrum of the H₃O⁺ Ion in Acid
462 Hydrates. *Journal of Chemical Physics*, *21*, 1421. <https://doi.org/10.1063/1.1699260>

463 Bolfan-Casanova, N., Keppler, H., & Rubie, D. C. (2003). Water partitioning at 660 km depth
464 and evidence for very low water solubility in magnesium silicate perovskite. *Geophysical
465 Research Letters*, *30*(17), 1905. <https://doi.org/10.1029/2003GL017182>

466 Cabral, R. A., Jackson, M. G., Koga, K. T., Rose-koga, E. F., Hauri, E. H., Whitehouse, M. J., et

- 467 al. (2014). Volatile cycling of H₂O, CO₂, F, and Cl in the HIMU mantle: A new window
468 provided by melt inclusions from oceanic hot spot lavas at Mangaia, Cook Islands.
469 *Geochemistry Geophysics Geosystems*, 15, 4445–4467.
470 <https://doi.org/10.1002/2014GC005473>.Received
- 471 Caracas, R., & Boffa Ballaran, T. (2010). Elasticity of (K,Na)AlSi₃O₈ hollandite from lattice
472 dynamics calculations. *Physics of the Earth and Planetary Interiors*, 181(1–2), 21–26.
473 Retrieved from <http://dx.doi.org/10.1016/j.pepi.2010.04.004>
- 474 Chantel, J., Manthilake, G., Andrault, D., Novella, D., Yu, T., & Wang, Y. (2016). Experimental
475 evidence supports mantle partial melting in the asthenosphere. *Science Advances*, 2(5),
476 e1600246.
- 477 Cynn, H., & Hofmeister, A. M. (1994). High-pressure IR spectra of lattice modes and OH
478 vibrations in Fe-bearing wadsleyite. *Journal of Geophysical Research*, 99(B9), 17717–
479 17727. <https://doi.org/10.1029/94jb01661>
- 480 Deschamps, F., Kaminski, E., & Tackley, P. J. (2011). A deep mantle origin for the primitive
481 signature of ocean island basalt. *Nature Geoscience*, 4(11), 1–4.
482 <https://doi.org/10.1038/ngeo1295>
- 483 Dixon, J. E., Leist, L., Langmuir, C., & Schilling, J. (2002). Recycled dehydrated lithosphere
484 observed in plume-influenced mid-ocean-ridge basalt. *Nature*, 420, 385–389.
- 485 Fei, H., Druzhbin, D., & Katsura, T. (2020). The Effect of Water on Ionic Conductivity in
486 Olivine. *Journal of Geophysical Research: Solid Earth*, 125(3).
487 <https://doi.org/10.1029/2019JB019313>
- 488 Ferroir, T., Onozawa, T., Yagi, T., Merkel, S., Miyajima, N., Nishiyama, N., et al. (2006).
489 Equation of state and phase transition in KAlSi₃O₈ hollandite at high pressure. *American*

- 490 *Mineralogist*, 91, 327–332. <https://doi.org/10.2138/am.2006.1879>
- 491 Freitas, D., & Manthilake, G. (2019). Electrical conductivity of hydrous silicate melts :
492 Implications for the bottom-up hydration of Earth ' s upper mantle. *Earth and Planetary*
493 *Science Letters*, 523, 115712. <https://doi.org/10.1016/j.epsl.2019.115712>
- 494 Freitas, D., Manthilake, G., Schiavi, F., Chantel, J., Bolfan-Casanova, N., Bouhfid, M. A., &
495 Andraut, D. (2017). Experimental evidence supporting a global melt layer at the base of the
496 Earth's upper mantle. *Nature Communications*, 8(1), 2186. [https://doi.org/10.1038/s41467-](https://doi.org/10.1038/s41467-017-02275-9)
497 [017-02275-9](https://doi.org/10.1038/s41467-017-02275-9)
- 498 French, S. W., & Romanowicz, B. (2015). Broad plumes rooted at the base of the Earth's mantle
499 beneath major hotspots. *Nature*, 525(7567), 95–99. <https://doi.org/10.1038/nature14876>
- 500 Fu, S., Yang, J., Karato, S. ichiro, Vasiliev, A., Presniakov, M. Y., Gavriiliuk, A. G., et al.
501 (2019). Water Concentration in Single-Crystal (Al,Fe)-Bearing Bridgmanite Grown From
502 the Hydrous Melt: Implications for Dehydration Melting at the Topmost Lower Mantle.
503 *Geophysical Research Letters*, 46(17–18), 10346–10357.
504 <https://doi.org/10.1029/2019GL084630>
- 505 Furusawa, S., Suemoto, T., & Ishigame, M. (1988). Quasielastic light scattering in the one-
506 dimensional superionic conductor hollandites. *Physical Review B*, 38(17), 12600–12606.
- 507 Gréaux, S., Kono, Y., Wang, Y., Yamada, A., Zhou, C., Jing, Z., et al. (2016). Sound velocities
508 of aluminum-bearing stishovite in the mantle transition zone. *Geophysical Research Letters*,
509 43, 4239–4246. <https://doi.org/10.1002/2016GL068377>.Received
- 510 Hacker, B. R. (2008). H2O subduction beyond arcs. *Geochemistry Geophysics Geosystems*, 9(3),
511 Q03001. <https://doi.org/10.1029/2007GC001707>
- 512 Hart, S. R. (1988). Heterogeneous mantle domains : signatures , genesis and mixing

- 513 chronologies. *Earth and Planetary Science Letters*, 90, 273–296.
- 514 Hart, S. R., Hauri, E. H., Oschmann, L. A., & Whitehead, J. A. (1992). Mantle Plumes and
515 Entrainment : Isotopic Evidence. *Science*, 256, 517–521.
- 516 He, Y., Sun, Y., Lu, X., Gao, J., Li, H., & Li, H. (2016). First-principles prediction of fast
517 migration channels of potassium ions in KAlSi₃O₈ hollandite: Implications for high
518 conductivity anomalies in subduction zones. *Geophysical Research Letters*, 43(12), 6228–
519 6233. <https://doi.org/10.1002/2016GL069084>.Received
- 520 van der Hilst, R. D., Widiyantoro, S., & Engdahl, E. R. (1997). Evidence for deep mantle
521 circulation from global tomography. *Nature*, 386, 578–584. Retrieved from
522 <http://dx.doi.org/10.1038/386578a0>
- 523 Hirschmann, M. M. (2006). Water, Melting, and the Deep Earth H₂O Cycle. *Annual Review of*
524 *Earth and Planetary Sciences*, 34(1), 629–653.
525 <https://doi.org/10.1146/annurev.earth.34.031405.125211>
- 526 Hu, H., Li, H., Dai, L., Shan, S., & Zhu, C. (2013). Electrical conductivity of alkali feldspar solid
527 solutions at high temperatures and high pressures. *Physics and Chemistry of Minerals*,
528 40(1), 51–62. <https://doi.org/10.1007/s00269-012-0546-4>
- 529 Huang, X., Xu, Y., & Karato, S. (2005). Water content in the transition zone from electrical
530 conductivity of wadsleyite and ringwoodite. *Nature*, 434(7034), 746–749.
531 <https://doi.org/10.1038/nature03426>
- 532 Ichiki, M., Baba, K., Obayashi, M., & Utada, H. (2006). Water content and geotherm in the
533 upper mantle above the stagnant slab : Interpretation of electrical conductivity and seismic
534 P-wave velocity models. *Physics of the Earth and Planetary Interiors*, 155, 1–15.
535 <https://doi.org/10.1016/j.pepi.2005.09.010>

- 536 Irifune, T., Ringwood, A. E., & Hibberson, W. O. (1994). Subduction of continental crust and
537 terrigenous and pelagic sediments: an experimental study. *Earth and Planetary Science*
538 *Letters*, *126*, 351–368.
- 539 Katsura, T., Sato, K., & Ito, E. (1998). Electrical conductivity of silicate perovskite at lower-
540 mantle conditions. *Nature*, *395*(October), 493–495. <https://doi.org/10.1038/26736>
- 541 Katsura, T., Yoneda, A., Yamazaki, D., Yoshino, T., Ito, E., Suetsugu, D., et al. (2010).
542 Adiabatic temperature profile in the mantle. *Physics of the Earth and Planetary Interiors*,
543 *183*(1–2), 212–218. <https://doi.org/10.1016/j.pepi.2010.07.001>
- 544 Kawai, K., & Tsuchiya, T. (2013). First-principles study on the high-pressure phase transition
545 and elasticity of KAlSi_3O_8 hollandite. *American Mineralogist*, *98*, 207–218.
546 <https://doi.org/10.2138/am.2007.2246>
- 547 Kelbert, A., Schultz, A., & Egbert, G. (2009). Global electromagnetic induction constraints on
548 transition-zone water content variations. *Nature*, *460*(7258), 1003–1006.
549 <https://doi.org/10.1038/nature08257>
- 550 Khanna, S. K., Gruner, G., Orbach, R., & Beyeler, H. U. (1981). Thermally Activated
551 Microwave Conductivity in the Superionic Conductor Hollandite
552 ($\text{K}_{1.54}\text{Mg}_{0.77}\text{Ti}_{7.23}\text{O}_{16}$). *Physical Review Letters*, *47*(4), 255–257.
- 553 Koch-Müller, M., & Rhede, D. (2010). IR absorption coefficients for water in nominally
554 anhydrous high-pressure minerals. *American Mineralogist*, *95*(5–6), 770–775.
555 <https://doi.org/10.2138/am.2010.3358>
- 556 Litasov, K. D., Kagi, H., Shatskiy, A., Ohtani, E., Lakshtanov, D. L., Bass, J. D., & Ito, E.
557 (2007). High hydrogen solubility in Al-rich stishovite and water transport in the lower
558 mantle. *Earth and Planetary Science Letters*, *262*, 620–634.

- 559 <https://doi.org/10.1016/j.epsl.2007.08.015>
- 560 Manthilake, G., Matsuzaki, T., Yoshino, T., Yamashita, S., Ito, E., & Katsura, T. (2009).
561 Electrical conductivity of wadsleyite as a function of temperature and water content.
562 *Physics of the Earth and Planetary Interiors*, 174(1–4), 10–18.
563 <https://doi.org/10.1016/j.pepi.2008.06.001>
- 564 Manthilake, G., Mookherjee, M., Bolfan-Casanova, N., & Andraut, D. (2015). Electrical
565 conductivity of lawsonite and dehydrating fluids at high pressures and temperatures.
566 *Geophysical Research Letters*, 42(18), 7398–7405. <https://doi.org/10.1002/2015GL064804>
- 567 Miura, H. (1986). The crystal structure of hollandite. *Mineralogical Journal*, 13(3), 119–129.
- 568 Mookherjee, M., & Steinle-Neumann, G. (2009). Detecting deeply subducted crust from the
569 elasticity of hollandite. *Earth and Planetary Science Letters*, 288(3–4), 349–358.
570 <https://doi.org/10.1016/j.epsl.2009.09.037>
- 571 Ni, H., Keppler, H., Manthilake, M. A. G. M., & Katsura, T. (2011). Electrical conductivity of
572 dry and hydrous NaAlSi₃O₈ glasses and liquids at high pressures. *Contributions to*
573 *Mineralogy and Petrology*, 162(3), 501–513. <https://doi.org/10.1007/s00410-011-0608-5>
- 574 Nishi, M., Irifune, T., Tsuchiya, J., Tange, Y., Nishihara, Y., Fujino, K., & Higo, Y. (2014).
575 Stability of hydrous silicate at high pressures and water transport to the deep lower mantle.
576 *Nature Geoscience*, 7, 224–227. <https://doi.org/10.1038/NGEO2074>
- 577 Nishiyama, N., Rapp, R. P., Irifune, T., Sanehira, T., Yamazaki, D., & Funakoshi, K. I. (2005).
578 Stability and P – V – T equation of state of KAlSi₃O₈ -hollandite determined by in situ X-
579 ray observations and implications for dynamics of subducted continental crust material.
580 *Physics and Chemistry of Minerals*, 32, 627–637. <https://doi.org/10.1007/s00269-005-0037->
581 y

- 582 Ohta, K., Hirose, K., Ichiki, M., Shimizu, K., Sata, N., & Ohishi, Y. (2010). Electrical
583 conductivities of pyrolitic mantle and MORB materials up to the lowermost mantle
584 conditions. *Earth and Planetary Science Letters*, 289(3–4), 497–502.
585 <https://doi.org/10.1016/j.epsl.2009.11.042>
- 586 Pamato, M. G., Myhill, R., Boffa Ballaran, T., Frost, D. J., Heidelbach, F., & Miyajima, N.
587 (2014). Lower-mantle water reservoir implied by the extreme stability of a hydrous
588 aluminosilicate. *Nature Geoscience*, 8, 75–79. <https://doi.org/10.1038/NGEO2306>
- 589 Rodriguez-Carvajal, J. (1993). Recent advances in magnetic structure determination by neutron
590 powder diffraction. *Physica B: Condensed Matter*, 192, 55–69.
- 591 Schiavi, F., Bolfan-Casanova, N., Withers, A. C., Médard, E., Laumonier, M., Laporte, D., et al.
592 (2018). Water quantification in silicate glasses by Raman spectroscopy: Correcting for the
593 effects of confocality, density and ferric iron. *Chemical Geology*, 483(March), 312–331.
594 <https://doi.org/10.1016/j.chemgeo.2018.02.036>
- 595 Schmidt, M. W. (1996). Experimental Constraints on Recycling of Potassium from Subducted
596 Oceanic Crust. *Science*, 272(5270), 1927–1930.
597 <https://doi.org/10.1126/science.272.5270.1927>
- 598 Sinmyo, R., Pesce, G., Greenberg, E., McCammon, C., & Dubrovinsky, L. (2014). Lower mantle
599 electrical conductivity based on measurements of Al, Fe-bearing perovskite under lower
600 mantle conditions. *Earth and Planetary Science Letters*, 393, 165–172.
601 <https://doi.org/10.1016/j.epsl.2014.02.049>
- 602 Smyth, J. R., & Jacobsen, S. D. (2006). Nominally anhydrous minerals and Earth 's deep water
603 cycle. (S. van der Lee & S. D. Jacobsen, Eds.), *American Geophysical Union Monograph*
604 *Series*. Washington DC: American Geophysical Union.

- 605 Sueda, Y., Irifune, T., Nishiyama, N., Rapp, R. P., Ferroir, T., Onozawa, T., et al. (2004). A new
606 high-pressure form of KAlSi_3O_8 under lower mantle conditions. *Geophysical Research*
607 *Letters*, *31*(23), 1–4. <https://doi.org/10.1029/2004GL021156>
- 608 Syracuse, E. M., Keken, P. E. Van, Abers, G. A., van Keken, P. E., Abers, G. A., Suetsugu, D.,
609 et al. (2010). The global range of subduction zone thermal models. *Physics of the Earth and*
610 *Planetary Interiors*, *183*(1–2), 73–90. <https://doi.org/10.1016/j.pepi.2010.02.004>
- 611 Tarits, P., & Mandéa, M. (2010). The heterogeneous electrical conductivity structure of the
612 lower mantle. *Physics of the Earth and Planetary Interiors*, *183*, 115–125.
613 <https://doi.org/10.1016/j.pepi.2010.08.002>
- 614 Urakawa, S., Kondo, T., Igawa, N., Shimomura, O., & Ohno, H. (1994). Synchrotron Radiation
615 Study on the High-Pressure and High-Temperature Phase Relations of KAlSi_3O_8 . *Physics*
616 *and Chemistry of Minerals*, *21*, 387–391.
- 617 Weidner, D. J., Li, L., Whitaker, M. L., & Triplett, R. (2018). Ultrasonic Acoustic Velocities
618 During Partial Melting of a Mantle Peridotite KLB-1. *Journal of Geophysical Research:*
619 *Solid Earth*, *123*(2), 1252–1261. <https://doi.org/10.1002/2017JB014753>
- 620 Willbold, M., & Stracke, A. (2006). Trace element composition of mantle end-members:
621 Implications for recycling of oceanic and upper and lower continental crust. *Geochemistry*
622 *Geophysics Geosystems*, *7*, Q04004. <https://doi.org/10.1029/2005GC001005>
- 623 Yoshikado, S., Ohachi, T., Taniguchi, I., Onoda, Y., Watanabe, M., & Fujiki, Y. (1982). Ionic
624 conductivity of hollandite type compounds from 100 Hz to 37.0 GHz. *Solid State Ionics*, *7*,
625 335–344.
- 626 Yoshino, T., Manthilake, G., Matsuzaki, T., & Katsura, T. (2008). Dry mantle transition zone
627 inferred from the conductivity of wadsleyite and ringwoodite. *Nature*, *451*(7176), 326–329.

628 <https://doi.org/10.1038/nature06427>

629 Yoshino, T., Nishi, M., Matsuzaki, T., Yamazaki, D., & Katsura, T. (2008). Electrical
630 conductivity of majorite garnet and its implications for electrical structure in the mantle
631 transition zone. *Physics of the Earth and Planetary Interiors*, 170(3–4), 193–200.

632 <https://doi.org/10.1016/j.pepi.2008.04.009>

633 Yoshino, T., Shimojuku, A., & Li, D. (2014). Electrical conductivity of stishovite as a function
634 of water content. *Physics of the Earth and Planetary Interiors*, 227, 48–54.

635 <https://doi.org/10.1016/j.pepi.2013.12.003>

636 Yoshino, T., Kamada, S., Zhao, C., Ohtani, E., & Hirao, N. (2016). Electrical conductivity model
637 of Al-bearing bridgmanite with implications for the electrical structure of the Earth's lower
638 mantle. *Earth and Planetary Science Letters*, 434, 208–219.

639 <https://doi.org/10.1016/j.epsl.2015.11.032>

640

641

642

643

644

645

646

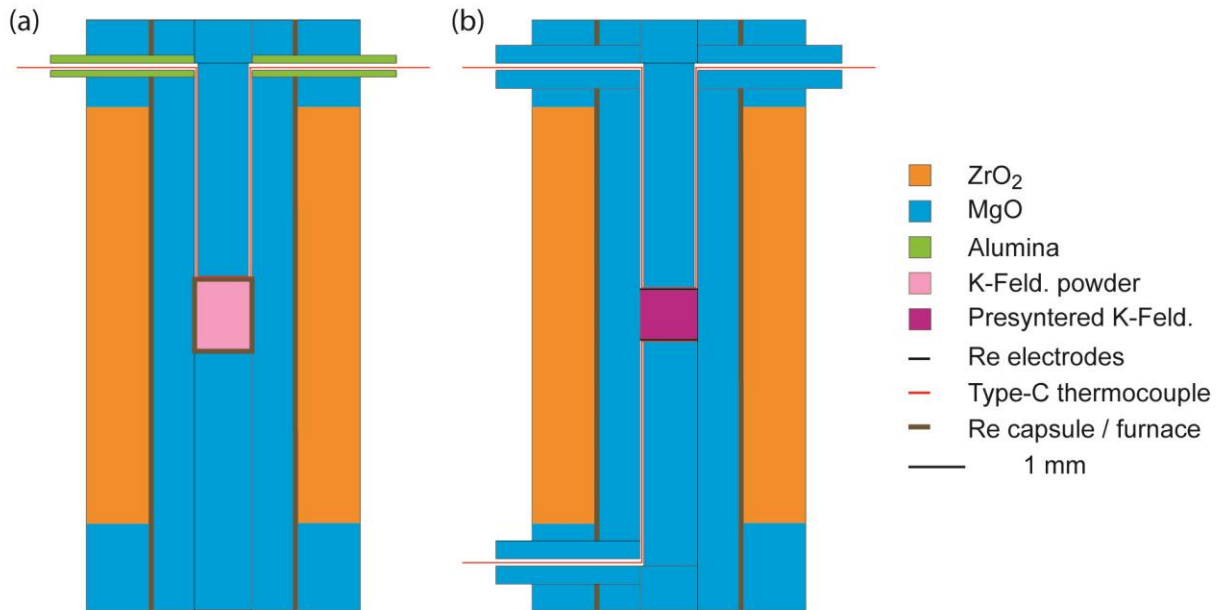
647

648

649

650

651 **Figures**



652

653 **Fig.1. A schematic cross-section of the assembly. (a) Used for the synthesis of K-feldspar. (b)**

654 **For electrical conductivity measurements at high-pressure and high-temperature. The three-**

655 **electrode configuration for electrical conductivity, which designed to avoid electrode leads sharing**

656 **the same tungsten carbide anvil in the KAWAI-cell, is expected to improve the insulation**

657 **resistance of the assembly.**

658

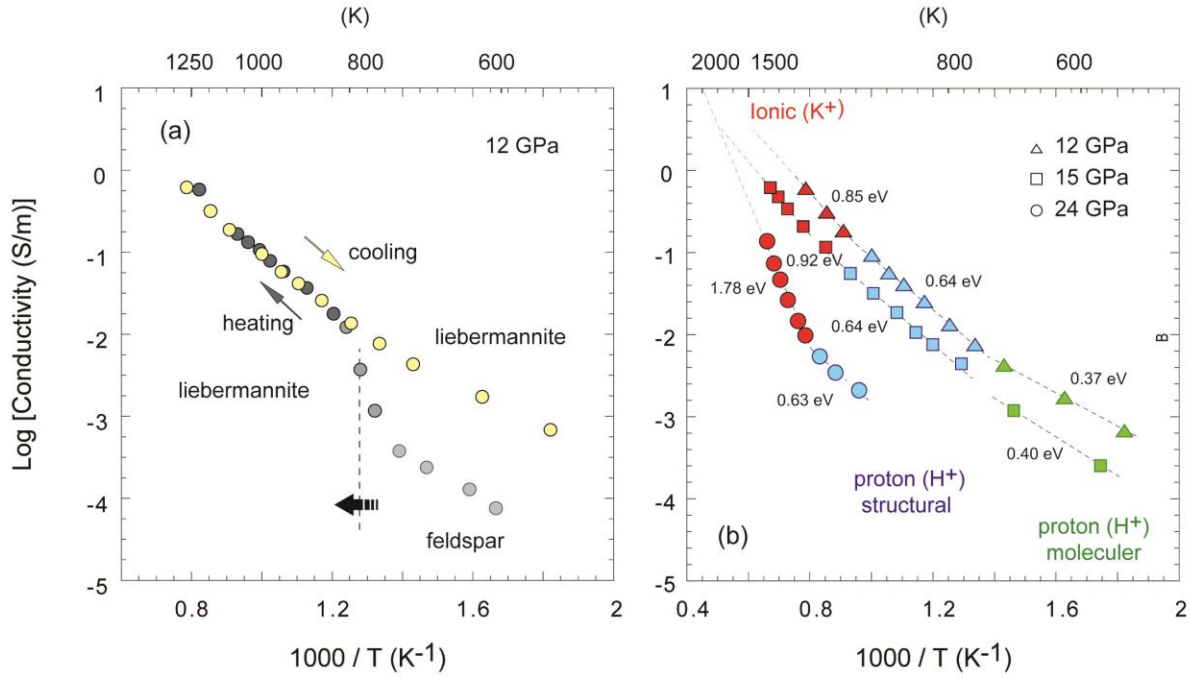
659

660

661

662

663



664

665 **Fig. 2. The electrical conductivity of liebermannite as a function of inverse temperature. (a)**

666 A plot of the logarithm of electrical conductivity as a function of inverse temperature. The

667 transformation of K-feldspar to liebermannite occurred above 600 K resulting in more than one

668 order of magnitude increase of conductivity. (b) Liebermannite at pressures 12, 15, and 24 GPa.

669 Different conduction mechanisms are labeled in different colors. The activation enthalpies are

670 shown next to individual fitting lines. The error bars associated with the electrical conductivity

671 data measurements are less than the symbol size at high temperatures.

672

673

674

675

676

677
 678
 679
 680
 681
 682
 683
 684
 685
 686
 687
 688
 689
 690
 691
 692
 693
 694
 695
 696
 697
 698
 699

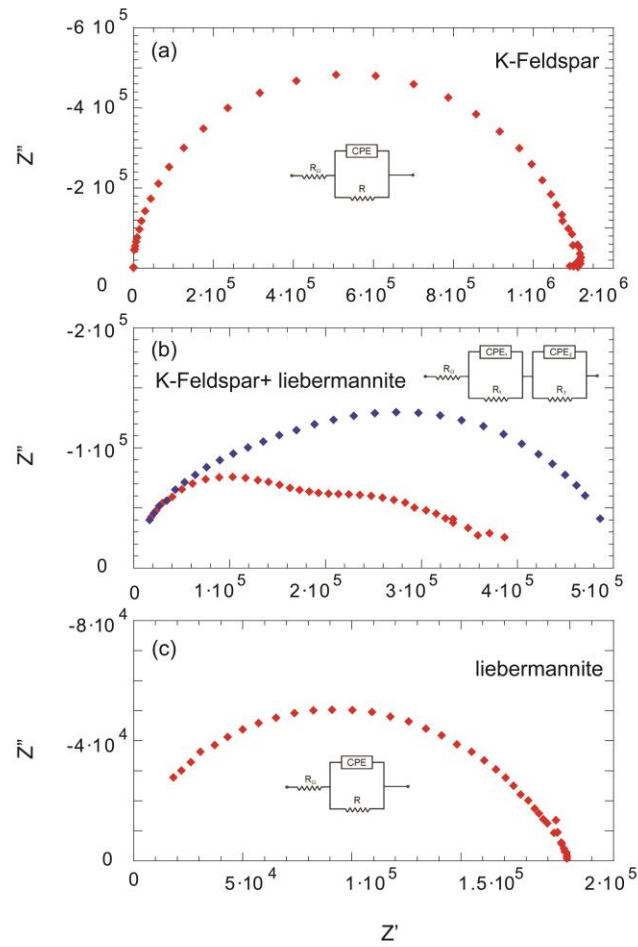


Fig. 3. Impedance spectra of the sample at different stages of heating at 12 GPa. (a) at 500 K electrical conductivity of K-feldspar before transforming into liebermannite, (b) at 718 K and 750 K, on the onset of the phase transformation, the second arc in the spectra develops. These additional arcs correspond to the formation of liebermannite. (c) At 850 K, after the complete transformation into liebermannite, there is a significant increase in the sample resistance. The sample resistance is due to the single conductive liebermannite phase. The corresponding equivalent circuit.

700
701
702
703
704
705
706
707
708
709
710
711
712
713
714
715
716
717
718
719
720
721
722

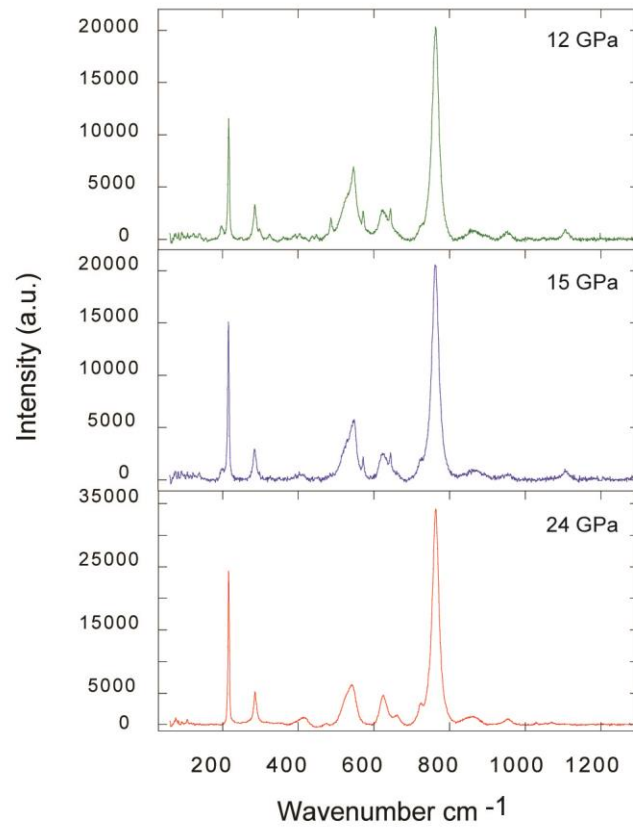


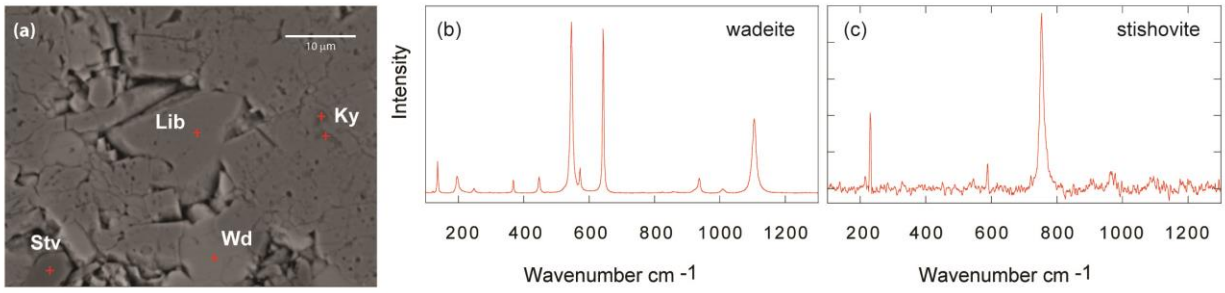
Fig. 4. Raman spectra of liebermannite at 12, 15, and 24 GPa.

723

724

725

726



727

728 **Fig. 5. Mineral assemblages of the recovered sample.** (a) A back-scattered electron image

729 showing the mineral assemblage at 15 GPa. (b, c) Low-wavenumber bands corresponding to

730 vibrations of the alumino-silicate network; (b) wadeite, (c) stishovite.

731

732

733

734

735

736

737

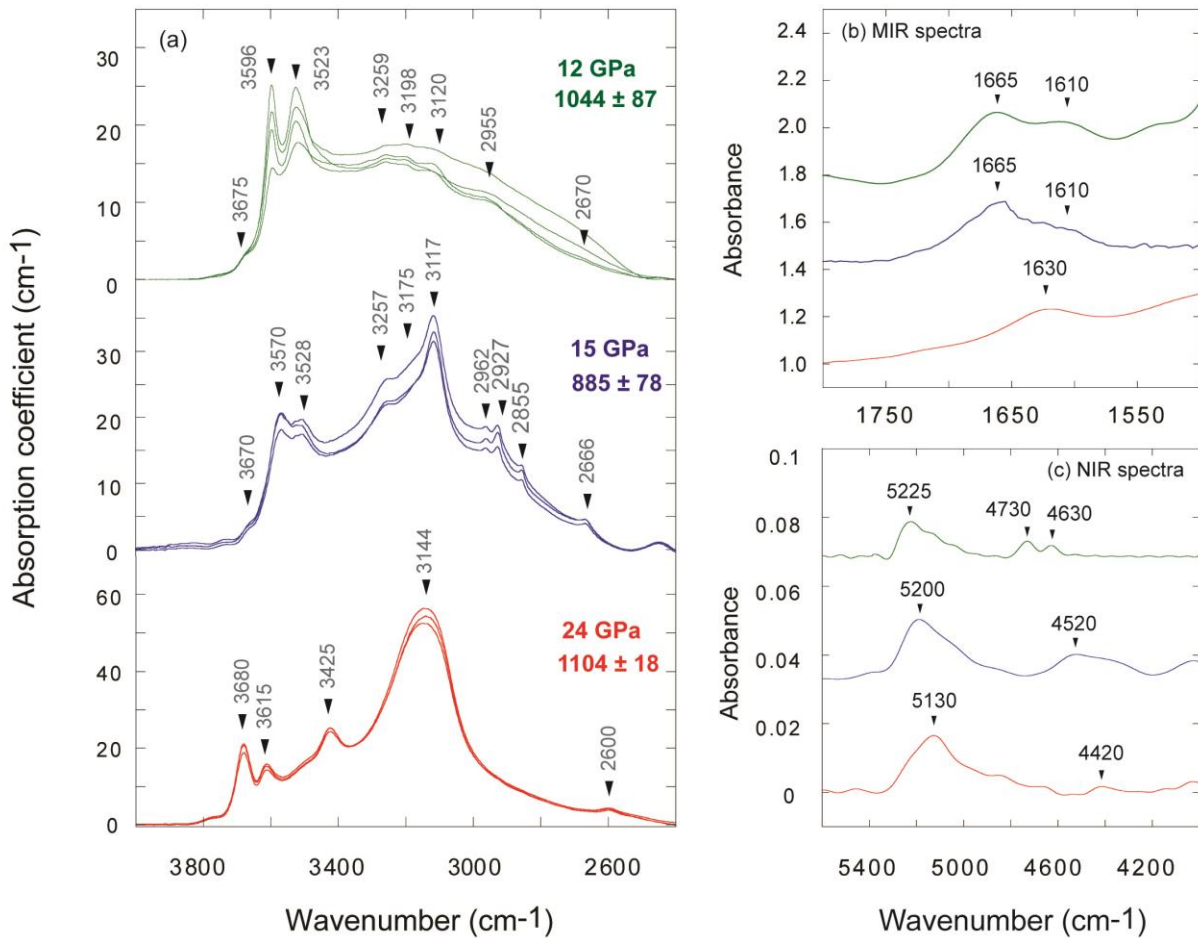
738

739

740

741

742



743

744

745

746 **Fig. 6. FTIR spectra of liebermannite.** (a) Near IR spectra of samples synthesized at 12 (green
 747 lines), 15 (blue lines), and 24 (red lines) GPa. The calculated H₂O contents (ppm wt.) are indicated
 748 next to spectra. (b) Middle IR spectra of the three samples showing bending modes of H₂O
 749 molecules and H₃O⁺ ions. (c) High-wavenumber IR region displaying bands at ~5200 (stretching
 750 vibrations of H₂O) and 4500-4700 cm⁻¹ (O-H stretching vibrations). The peak at 4170 cm⁻¹ could
 751 be related to H-H vibrations.

752
753
754
755
756
757
758
759
760
761
762
763
764
765
766
767
768
769
770
771
772
773
774

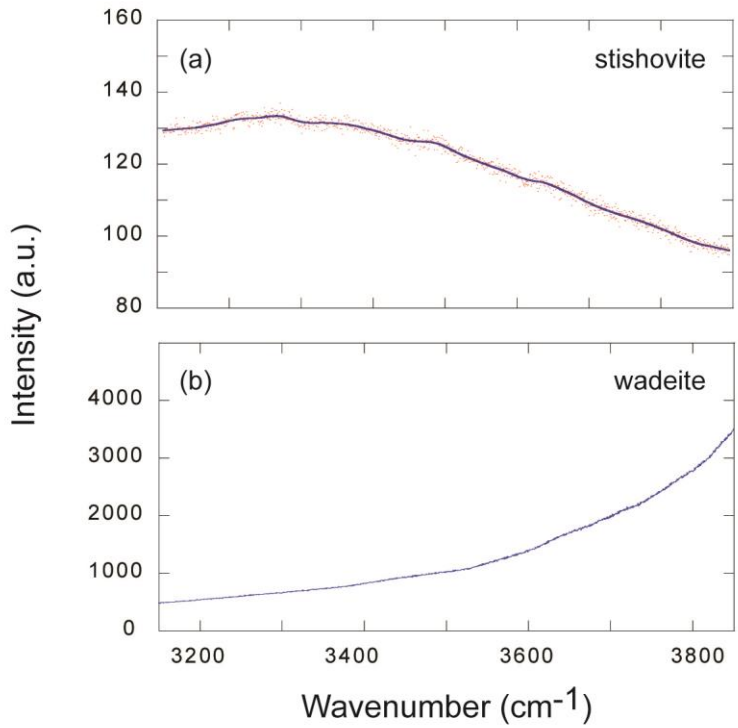


Fig. 7. Raman spectra of minor phases observed at the sample synthesized at 15 GPa. The background uncorrected Raman spectra in the O-H region of stishovite (a) and wadeite (b), co-existing with liebermannite. The background noise of the Raman spectrum of stishovite was smoothed using the loess regression method shown in the blue line. Both indicate water absent conditions in their crystal structure. Raman analyses of kyanite were not possible due to their small grain sizes.

775
776
777
778
779
780
781
782
783
784
785
786
787
788
789
790
791
792
793
794
795
796
797
798

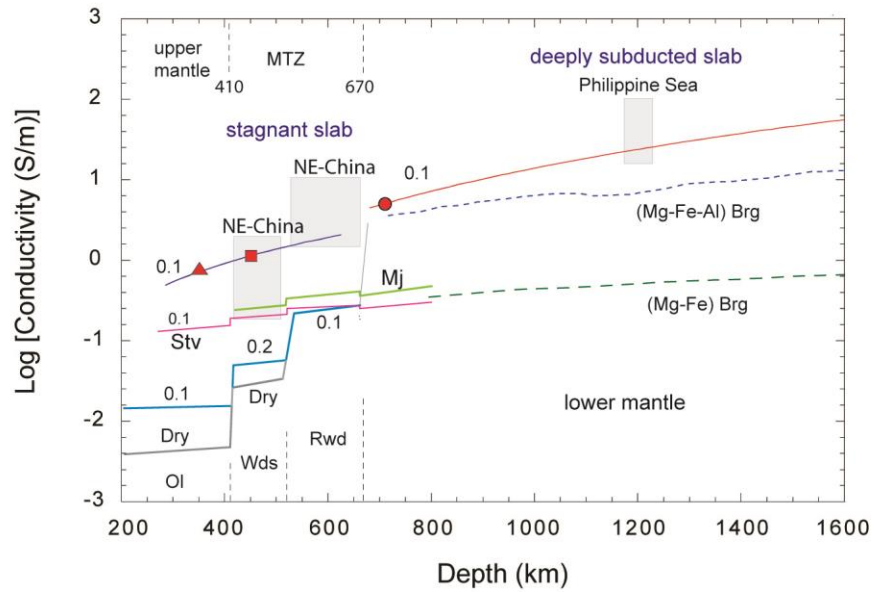
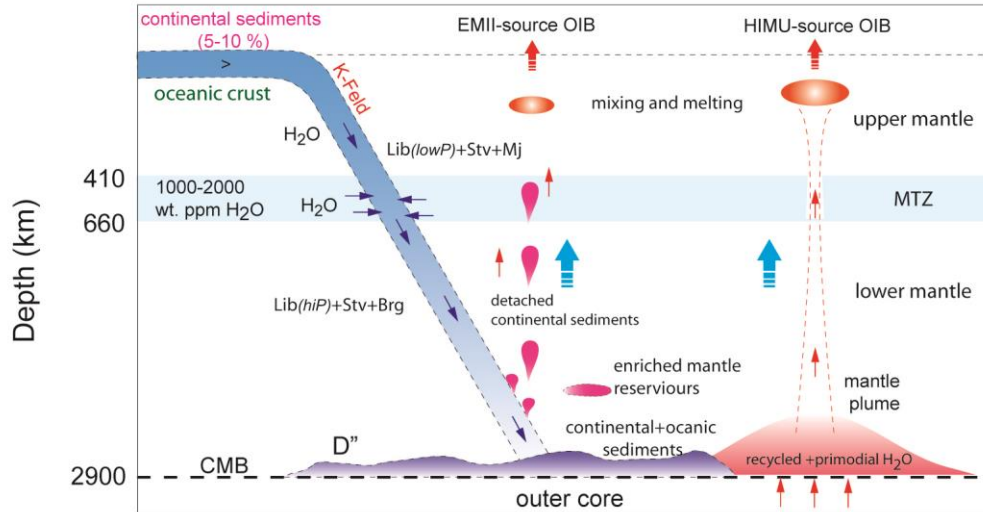


Fig. 8. Comparison of electrical conductivities of liebermannite with global and regional electrical conductivity profiles. The blue and red lines correspond to the extrapolation of electrical conductivity along the relevant subduction geotherms (Syracuse et al., 2010), and along the adiabatic geotherm in the lower mantle (Katsura et al., 2010), respectively. The red shaded triangle, square, and the circle indicate the electrical conductivity of liebermannite at 12, 15, and 24 GPa, respectively. The gray shaded boxes indicate the conductivity profiles of NE-China (Kelbert et al., 2009) and the Philippine Sea (Tarits & Mandéa, 2010). The electrical conductivity profiles of dry (black lines) and wet (blue lines) olivine, wadsleyite, ringwoodite (Yoshino et al., 2008), stishovite with 0.1 wt% of H₂O (Yoshino et al., 2014) (pink lines) and majorite garnet (Yoshino et al., 2008) (light green lines) are shown for comparison. The electrical conductivity of (Mg, Fe) bridgmanite (Katsura et al., 1998) (green dashed line) and (Mg, Fe, Al) bridgmanite (Ohta et al., 2010; Sinmyo et al., 2014; Yoshino et al., 2016) (blue dashed line), extrapolated along the adiabatic geotherm in the lower mantle (Katsura et al., 2010), are shown for comparison. The numbers next to conductivity lines are the water contents in wt. %.

799
800
801
802
803
804
805
806



807 **Fig. 9. The potential mechanism explaining the elevated H₂O content in ocean island basalts.**

808 K-feldspar in subducting continental sediments transforms to liebermannite above 8 GPa and
 809 continues to be stable down to the core-mantle boundary conditions. Most of the H₂O carried to
 810 the lower mantle by deep penetrating slabs may have been incorporated into the slab at the surface.
 811 However, due to the imbalance of the mass of H₂O transported to the Mantle Transition Zone
 812 (MTZ) via subduction (Hacker, 2008) and the estimated mass of H₂O stored in MTZ based on
 813 H₂O contents of constituent phases (Freitas & Manthilake, 2019), extraction of H₂O from MTZ
 814 to the lower mantle can be expected. Because of the ability of liebermannite to accommodate several
 815 wt. % of the water in its structure (both in lattice defects and the tunnel structures), we argue that
 816 liebermannite could be a possible carrier of water from the MTZ to the lower mantle. In this two-
 817 step, H₂O conveyor process, the extraction of H₂O by rehydration of deep penetrating slabs at the
 818 MTZ would be a likely scenario. Depending on gravitational stability, the subducting continental
 819 sediment component may detach from deep-extending slabs, rise through the mantle forming
 820 EMII-source OIB, in which liebermannite is the principal water carrier. Some continental
 821 sediments may reach the CMB and provide H₂O for HIMU-source lower mantle-derived plumes.
 822 (Lib: liebermannite, Sa: K-feldspar, Mj: majorite garnet, Brg: bridgmanite, Stv; stishovite).

823
824
825

826 **List of tables**

827

Table 1. The reference pre-exponential factor $\text{Log } \sigma_0$ and the activation enthalpy in eV for liebermannite at 12, 15, and 24 GPa and their respective water contents.

Pressure (GPa)	Temperature (K)	Log σ_0 *	Log σ_0 **	ΔH *	ΔH **	H ₂ O contents ppm wt.
12	550 -750	0.57	n.a	0.37	n.a.	1044 ± 87
	750 - 1100	2.19	2.32	0.64	0.78	
	>1100	3.14	3.88	0.85	0.82	
15	573 - 683	0.58	n.a	0.4	n.a.	885 ± 78
	773 -1173	1.76	1.61	0.64	0.76	
	> 1173	2.78	3.96	0.92	0.83	
24	1040 - 1200	0.38	0.24	0.63	0.76	1104 ± 18
	> 1270	5	8.26	1.78	0.89	

* parameters from individual fitting

** parameters from single fit

n.a: not nalyzed

828

829 **Table 2.** Chemical composition of the constituent mineral phases.

830

831

832

833

834

835

836

837

838

839

840

841

842

843

844

845

846

847

848

849

Table 2. Chemical composition of the constituent mineral phases.

	Liebermannite			Wadeite		Stishovite		Kyanite	
	12 GPa	15 GPa	24 GPa	12 GPa	15 GPa	12 GPa	15 GPa	12 GPa	15 GPa
SiO₂	64.44 (0.7)	63.91 (2.5)	66.70 (0.2)	73.00 (0.9)	71.82 (0.5)	100.50 (0.8)	101.13 (0.5)	38.23 (0.9)	39.11 (0.9)
K₂O	16.47 (0.4)	16.18 (1.2)	16.42 (1.8)	27.16 (0.8)	28.22 (0.6)	0.06 (0.3)	0.13 (0.07)	0.15 (0.06)	0.61 (0.4)
Al₂O₃	18.98 (0.3)	20.4 (2.9)	17.21 (2.0)	0.15 (0.1)	0.6 (0.5)	0.05 (0.2)	0.07 (0.03)	62.6 (1.2)	61.35 (1.2)
Total	99.89	100.49	100.33	100.31	100.64	100.62	101.33	100.98	101.07

The standard deviation indicated in parenthesis.

850